# Power balance of negative-glow electrons

J. E. Lawler and E. A. Den Hartog
*Department of Physics, University of Wisconsin, Madison, Wisconsin 53706*

W. N. G. Hitchon
*Department of Electrical and Computer Engineering, University of Wisconsin, Madison, Wisconsin 53706*
(Received 26 November 1990)

Laser-induced fluorescence and absorption spectroscopy are used to study the mixing of populations of excited He atoms due to electron collisions in the negative glow of a dc He discharge. These measurements yield the density ($n_e^c \cong 5\times10^{11}$ cm$^{-3}$) and temperature (0.1 eV $\leq k_B T_e^c \leq$ 0.2 eV) of the low-energy (or "cold") electrons in the negative glow. The cold electrons are trapped in a potential-energy well. In a complementary investigation, Monte Carlo simulations are used to determine the density ($n_e^h \cong 10^9$ cm$^{-3}$) and temperature ($k_B T_e^h \cong 3$ eV) of the high-energy (or "hot") electrons in the negative glow. Results from the experiments and Monte Carlo simulations are combined to study the power balance of the cold trapped electrons. The cold-electron temperature is established by a balance between cooling from recoil during elastic collisions with neutral atoms, and heating due to Coulomb collisions with hot electrons. The linear variation of hot-electron density with discharge current density causes a linear variation in cold-electron temperature with current density. Hot electrons also excite metastable atoms to higher radiating levels to produce most of the light from the negative glow.

## I. INTRODUCTION

The cathode region of glow-discharge plasmas is of fundamental and practical interest. The proximity of the cathode and the large and rapidly varying electric fields result in electron-energy distributions that are not determined by the local $E/N$ (ratio of electric field to gas density). The failure of the widely used hydrodynamic equilibrium (or local-field) approximation means that a realistic model should be based on kinetic theory. Practical interest arises from the many important uses of glow-discharge plasmas.

The negative glow is the part of the cathode region immediately next to the high-field cathode fall. Although it has a very small electric field, it too is nonhydrodynamic because of a low density of high-energy electrons injected from the cathode fall region. Den Hartog, O'Brian, and Lawler recently described laser experiments that demonstrated the existence of a quite high density ($n_e^c = 5\times10^{11}$ cm$^{-3}$) of rather low-energy electrons ($k_B T_e^c = 0.12$ eV) in the negative glow of a He glow discharge at 0.846 mA/cm$^2$ and 3.50 Torr.[1] The electron density $n_e^c$ and temperature $T_e^c$ refer to the "cold" negative-glow electrons. The high-energy electrons injected from the cathode fall result in a distribution that is only partly described by a single Maxwellian. These laser experiments detected mixing of populations between excited levels of He caused by collisions between low-energy electrons and excited He atoms. Data from one exothermic (superelastic) and one endothermic (inelastic) reaction were combined to yield a density and temperature of the low-energy electrons.

Earlier measurements by Anderson on the negative glow of a comparable but not identical He discharge were based on probe and microwave techniques.[2] Anderson refers to the cold negative-glow electrons as "ultimate" electrons. He found a cold electron density of $8\times10^{11}$ cm$^{-3}$ for a He discharge at 4.0 Torr and 0.22 mA/cm.[2] Den Hartog, O'Brian, and Lawler observed $5\times10^{11}$ cm$^{-3}$ at 3.50 Torr and 0.846 mA/cm,[2] but with a somewhat different geometry. The temperatures measured by Anderson using a probe and microwave radiometry did not agree very well, but he seems to favor an even lower temperature ($k_B T_e^c = 0.034$ eV) than that reported by Den Hartog, O'Brian, and Lawler. Anderson also observed using a probe a density of $\sim1\times10^9$ cm$^{-3}$ of energetic electrons, which he called "secondary" electrons with a high temperature ($k_B T_e^h \simeq 4.3$ eV). Anderson, like some earlier authors, distinguished between secondary electrons and energetic "primary" electrons from the cathode fall. We will not make this distinction, but instead will refer to both secondary and primary electrons as high-energy or "hot" electrons.

Much of the research on the cathode region before Anderson's work is summarized in a review article by Francis.[3] These earlier studies on the negative glow, which were based on probes, apparently missed the cold electrons in the negative glow. More recent probe work is summarized in a review article by Emeleus.[4]

The cold electrons are trapped in a potential-energy well formed by a field reversal in the negative glow. There has been much discussion in review articles on the existence and location of a field reversal in the negative glow.[3-5] Most authors seem comfortable with a field reversal in the negative glow under a variety of conditions. A convincing theoretical treatment of the cathode-fall

 

and negative-glow regions that predicts the existence and location of the field reversal and other properties of the negative glow has been an elusive goal. A convincing theoretical treatment must avoid the many assumptions and approximation of older models.

It is difficult to directly measure the very small fields in the negative glow using either probe or spectroscopic techniques. In an important early work Druyvesteyn produced evidence for the field reversal by measuring the discharge voltage at fixed current while moving the anode into and through the negative glow.[6] Druyvesteyn's measurements, like more modern probe measurements, are rather invasive and thus perturb the discharge. Den Hartog, Doughty, and Lawler presented evidence for a field reversal in the negative glow of dc He discharges.[7] Their evidence is based on a comparison of Monte Carlo simulations of electron avalanches with an empirical current balance at the cathode. The current balance is the ratio of ion to electron current. Very few of the ions produced in the negative glow contribute to the ion current at the cathode in discharges studied by Den Hartog, Doughty, and Lawler.[7] The ionization in the negative glow produced by energetic electrons injected from the cathode fall must be balanced either by recombination or, if recombination is negligible, then by a drift of ions in a reversed field toward the anode. This drift is analogous to ambipolar diffusion. More recently Gottscho *et al.* have observed a change in the sign of an optogalvanic effect on molecular ion lines.[8] The sign change was correctly interpreted as due to a field reversal in the negative glow. The noninvasive optogalvanic technique for observing the field reversal is attractive because probes can represent a significant perturbation to the plasma, and because probe characteristics are difficult to interpret for non-Maxwellian, anisotropic electron-energy distributions.

A convincing theoretical treatment of the ionization balance, which would predict the field reversal and the density of the cold electrons, requires a self-consistent kinetic calculation. The convective scheme shows great promise of making such calculations possible for a variety of discharges in the near future.[9,10] The research described here focuses on identifying important physical processes such as those in the power balance of the cold negative-glow electrons. Section II is a detailed discussion of the laser experiments by Den Hartog, O'Brian, and Lawler which determined the density and temperature of the cold negative-glow electrons in a He discharge.[1] Section III describes a complementary investigation in which Monte Carlo simulations of electron avalanches in the same discharge are used to study the hot electrons in the negative glow. The simulations are quite realistic because they are based on empirical field maps, gas density measurements, and an excellent set of He cross sections. Section IV explores the power balance of the cold electrons by combining experimental results and Monte Carlo simulations. This work identifies the dominant physical processes, which maintain $k_B T_e^c$ between 0.1 and 0.2 eV. We find that the dominant cooling term in the power balance of the cold electrons is due to energy lost during elastic collisions with neutral atoms. We find that the dominant heating term in the power balance of the cold electrons is due to energy gain in Coulomb collisions with the hot negative-glow electrons. Section V explores the role of multistep excitation caused by hot electrons in producing light from the negative glow. Finally, Sec. VI summarizes our conclusions and outlines future work.

## II. EXPERIMENTS

Figure 1 is a schematic of the experimental apparatus. The discharge used in these studies is produced between flat, circular aluminum electrodes 3.2 cm in diameter and separated by 0.62 cm. The electrodes are water cooled to minimize gas heating and are backed by insulating ceramic annuli to prevent plasma from forming behind them. The discharge tube is constructed of glass and stainless steel. Most of the vacuum seals are made with knife-edge flanges on copper gaskets. The only exceptions are the high-vacuum epoxy seals around the fused silica Brewster windows and fluorescence port. A liquid-nitrogen-trapped diffusion pump evacuates the system to $2\times10^{-8}$ Torr. When no liquid nitrogen is in the trap the diffusion pump is valved off to prevent back-diffusion of oil into the system, and the vacuum is maintained with an ion pump. The leak rate into the sealed system is $\sim3\times10^{-4}$ Torr/day.

During discharge operation ultrahigh purity (99.9999 %) helium is slowly flowed through the system at a pressure of 3.50 Torr as measured with a capacitance monometer. The helium first passes through a cataphoresis discharge to remove any residual contaminants before entering the main discharge tube. Emission spectra reveal only weak aluminum and hydrogen impurity lines. The aluminum originates from the slow sputtering erosion of the cathode due to $He^+$ bombardment. This may also be the source of the hydrogen contamination since many metals absorb hydrogen. After being exposed to air the aluminum cathode forms an oxide layer that is subsequently removed by either operating an argon plasma (argon is very effective at sputtering) or lengthy

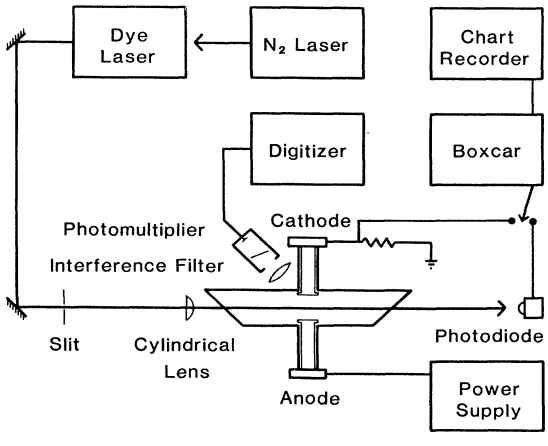


FIG. 1. Schematic of the apparatus. The fluorescence collection system based on an interference filter, rather than the 0.2-m monochromator, is shown in this schematic.

operation of a helium plasma. The removal of the oxide layer is evidenced by the appearance of the weak aluminum emission lines and a stabilizing of the *V-I* characteristics. A carefully prepared cathode results in *V-I* characteristics which are reproducible within a few precent over a period of several months.

Discharges at 3.50-Torr helium pressure over a range of current densities from 0.190 to 1.50 mA/cm$^2$ are studied. The low current density corresponds to a near-normal cathode-fall voltage of 175 V and the high current density corresponds to a highly abnormal cathode-fall voltage of 600 V. The discharge current is spread uniformly across the electrode surface.[7] In this paper measurements made at 0.846 mA/cm$^2$ current density and a cathode-fall voltage of 261 V are emphasized and analyzed in detail. Results at other current densities are reported only to illustrate trends.

The laser used is a $N_2$ laser pumped dye laser. The dye laser has a bandwidth of 0.2 cm$^{-1}$, pulse length of $\sim$3 ns, and it is tunable over a wavelength range of 360–700 nm. Frequency-doubling crystals are used to extend this range down to 205 nm. The laser beam is focused between the electrodes giving a spatial resolution of $\sim$0.2 mm. Spatial maps are made by translating the discharge tube on a precision translation stage.

Two laser-based diagnostics are used, which together yield $n_e^c$ and $T_e^c$ for the cold electrons in the negative glow. Each diagnostic provides an independent determination of the product of $n_e^c$ and a temperature-dependent rate constant. The first diagnostic, based on the endothermic electron collisional transfer between low Rydberg levels, yields a relation in which $n_e^c$ decreases with increasing $T_e^c$. A preliminary report of this diagnostic appears elsewhere;[1] a more complete discussion is included here. The second diagnostic is based on the spin conversion of helium metastable atoms,

$$\mathrm{He}(2\,^1S)+e^-\rightarrow\mathrm{He}(2\,^3S)+e^-+0.79\ \mathrm{eV}\ . \qquad (1)$$

This is an exothermic process and yields a relation in which $n_e^c$ increases with $T_e^c$. This diagnostic is described in detail elsewhere,[7] for completeness a brief description will be given here. The intersection of these two relations yields $n_e^c$ and $T_e^c$ for the cold electrons in the negative glow.

In the Rydberg atom diagnostic a low Rydberg level is selectively populated with the laser. The collision-induced transfer rate from the level populated by the laser to a higher-lying level is determined by measuring the ratio of the laser-induced fluorescence (LIF) signals from the two levels. Frequency doubling of the dye laser beam is necessary for excitation of low Rydberg levels out of the $2\,^3S$ metastable level. LIF is collected in a direction perpendicular to both the discharge axis and the laser axis. A spherical lens is used to image the laser-discharge interaction region onto the 0.25-mm entrance slit of a 0.2-m monochromator, which is used as a spectral filter. The $\sim$1-nm bandpass is necessary to isolate the triplet Rydberg level fluorescence from cascade fluorescence from lower-lying singlet levels. A 1P28A photomultiplier detects the filtered fluorescence. The base of the photomultiplier tube is wired for low inductance to maintain the full bandwidth of the tube. The photomultiplier signal is amplified by a factor of 100 and then digitized with a Transiac 2001S digitizer with a 4100 averaging memory interfaced to an IBM PC. Typically 5000 LIF pulses are averaged. The temporal integral of this average is the measured fluorescence $F$. The LIF signal from the upper Rydberg level is two to three orders of magnitude weaker than the signal from the level populated by the laser.

The Rydberg atom diagnostic works by populating a low-lying Rydberg level with principle quantum number $n$ by tuning the laser to the $2\,^3S\rightarrow n\,^3P$ transition. This is effectively populating the entire $n$ manifold because the different $l$ levels are highly coupled by neutral collisions at 3.50 Torr.[11] The population of each $l$ level is proportional to its degeneracy. The $s$ level may be an exception to this since for $n=5$ it lies $\sim 3k_BT$ below the $p$ level so that it may not be fully coupled to the rest of the manifold. Here $T$ is the gas temperature. For the purposes of this experiment the lack of coupling of the $s$ level is unimportant because the $s$ population is a small fraction of the total $n$ manifold population. The collisional transfer rate between two Rydberg manifolds $n$ and $n'$ $(n'>n)$ is determined by measuring the ratio of the LIF signals $n'\,^3D\rightarrow 2\,^3P$ and $n\,^3D\rightarrow 2\,^3P(F_{n'}/F_n)$ when the lower-lying manifold is populated with the laser.

Three transfer rates are measured. When the laser is tuned to the $2\,^3S\rightarrow 5\,^3P$ transition at 294.5-nm spatial maps of fluorescence are made from the $5\,^3D\rightarrow 2\,^3P(F_5)$ and $6\,^3D\rightarrow 2\,^3P$ $(F_6)$ transitions at 402.6 and 382.0 nm, respectively. $F_6/F_5$ yields the $n=5$ to 6 collision-induced transfer rate. When the laser is tuned to the $2\,^3S\rightarrow 6\,^3P$ transition at 282.9 nm fluorescence is mapped from the $6\,^3D\rightarrow 2\,^3P$, $7\,^3D\rightarrow 2\,^3P$, and $8\,^3D\rightarrow 2\,^3P$ transitions at 382.0, 370.5, and 363.4 nm, respectively. $F_7/F_6$ and $F_8/F_6$ yield the $n=6$ to 7 and the $n=6$ to 8 transfer rates, respectively. Figure 2 shows a plot of $F_8/F_6$ versus distance from the cathode. The left axis of the plot is the cathode position and the right side is the anode position. The position where the linearly decreasing cathode-fall field extrapolates to zero is indicated by the dashed vertical line on the plot.[7] This is the boundary between the cathode fall (CF) and negative glow (NG).

It will be shown in the discussion that follows that the lifetimes of the Rydberg manifolds $\tau_{n'}$ must be known in order to analyze the LIF maps. $\tau_{n'}$ is the lifetime of the manifold under discharge conditions (where the decay arises from both radiative and collisional effects). $\tau_{n'}$ is measured *in situ* by tuning the laser to the peak of the $2\,^3S\rightarrow n'\,^3P$ transition and collecting $n'\,^3D\rightarrow 2\,^3P$ fluorescence as described for the fluorescence mapping. The photomultiplier fluorescence signal is time resolved and analyzed with a Princeton Applied Research 162 and 165 boxcar averager with a 2-ns gate. The results of these measurements are $\tau_6=29.1$ ns, $\tau_7=30.8$ ns, and $\tau_8=33.9$ ns. The uncertainty in the lifetime measurements is 10%.

The Rydberg atom diagnostic is analyzed with a straightforward rate equation approach. The laser excitation of the $n$ manifold can be approximated as an instantaneous population excess at $t=0$, $N_n(0)$. The subse-

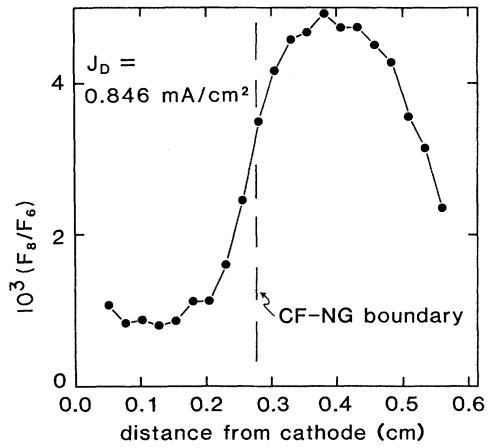


FIG. 2. Ratio of LIF signal from $n=8$ that from $n=6$ as a function of distance from the cathode.

quent decay of the manifold population is described by a single exponential $N_n(t)=N_n(0)\exp(-t/\tau_n)$, where $\tau_n$ is the lifetime of the $n$ manifold in the discharge environment. Under the same conditions, the population in the $n'$ manifold can be described by the rate equation

$$\frac{dN_{n'}(t)}{dt}=\frac{-N_{n'}(t)}{\tau_{n'}}+R_{nn'}N_n(t)\ , \tag{2}$$

where $\tau_{n'}$ is the lifetime of the $n'$ manifold and $R_{nn'}$ is the rate for collision induced transfer from manifold $n$ to $n'$, including both neutral and electron collisions. The rates due to ion collisions and due to hot-electron collisions are easily shown to be insignificant ($<10\%$). The solution to this equation is

$$N_{n'}(t)=\frac{R_{nn'}N_n(0)}{\tau_{n'}^{-1}-\tau_n^{-1}}(e^{-t/\tau_n}-e^{-t/\tau_{n'}})\ . \tag{3}$$

The ratio of the time-integrated fluorescence from the $n'$ manifold to that from the $n$ manifold is

$$\frac{F_{n'}}{F_n}=\frac{b_{n'}\epsilon_{n'}\tau_n^{-1}\int N_{n'}(t)dt}{b_n\epsilon_n\tau_n^{-1}\int N_n(t)dt}\ , \tag{4}$$

where $b_n$ is the branching ratio of the observed $n\,^3D\rightarrow 2\,^3P$ transition and $\epsilon$ is the collection efficiency of the detection system at the frequency of the $n\,^3D\rightarrow 2\,^3P$ transition. It is safe to assume that $\epsilon_n\approx\epsilon_{n'}$ since the frequencies of the observed transitions are nearly equal. The ratio $b_{n'}/b_n$ is given by

$$\frac{b_{n'}}{b_n}=\frac{n^2A_{n'd-2p}\tau_{n'}}{(n')^2A_{nd-2p}\tau_n}\ , \tag{5}$$

where $A$ is the radiative transition probability for the transition indicated and $n^2$ is the total degeneracy of the $n$ manifold. After substitution and integration $F_{n'}/F_n$ is given by

$$\frac{F_{n'}}{F_n}=\frac{n^2A_{n'd-2p}R_{nn'}\tau_{n'}}{(n')^2A_{nd-2p}}\ . \tag{6}$$

From this relation the collision-induced transfer rate can be calculated from the measured ratio of fluorescence. The values for the transition probabilities are taken from Wiese, Smith, and Glennon.[12]

Figure 2 shows the strong spatial asymmetry of the $F_{n'}/F_n$ ratio in the discharge. Throughout most of the cathode fall, to the left of the CF-NG boundary, the collisional transfer rate is low and does not vary as a function of position. The electron density is very low in the cathode fall and collision-induced transfers are due to neutral collisions. The neutral contribution to $R_{nn'}$ is constant as a function of position. The large enhancement of the collisional transfer rate to the right of the CF-NG boundary is due to collisions with the cold electrons trapped in the negative glow. The fact that this enhancement extends across the CF-NG boundary into the cathode fall may be due to population transfer caused by collision between hot electrons and Rydberg atoms. Table I lists the results of the $R_{nn'}$ determination for the three collision processes studied. The table gives a value for $(R_{nn'})_{CF}$, which is the average over the flat portion of the data in the cathode fall, and a value for $(R_{nn'})_{NG}-(R_{nn'})_{CF}$, which is the difference between the peak in the negative glow and the cathode-fall value. $(R_{nn'})_{CF}$ is the neutral collision transfer rate and $(R_{nn'})_{NG}-(R_{nn'})_{CF}$ is the rate due only to the negative-glow electrons. These values result from the average of two sets of data taken several weeks apart. The two data sets reproduced within 10%.

The measured electron-collision-induced transfer rate can be expressed as the product of a temperature-dependent rate constant $k_{nn'}(T_e^c)$ and the electron density $n_e^c$. The rate constants are taken from the analytical formula given by Vriens and Smeets.[13] In evaluating this formula for manifold-to-manifold collision-induced transfer, weighted averages are calculated for the energies of the manifolds and absorption oscillator strengths. The energies of individual levels are taken from Martin.[14] Level-to-level absorption oscillator strengths are taken from Kono and Hattori for $l<2$,[15] and hydrogenic values from Wiese, Smith, and Glennon are used for higher $l$.[12] The hydrogenic approximation is estimated to be within a few percent of helium oscillator strengths for $l\geq 2$. The resulting relations $n_e^c=k_{nn'}(T_e^c)/R_{nn'}$ are plotted as the thin lines in Fig. 3 for the three different col-

TABLE I. Collision-induced transfer rate $R_{nn'}$ in the 0.846-mA/cm$^2$ discharge for the three collision processes studied. $(R_{nn'})_{CF}$ is interpreted as the rate due to collisions with neutral atoms. $(R_{nn'})_{NG}-(R_{nn'})_{CF}$ is interpreted as the rate due to collisions with the low-energy electrons in the negative glow.

| $n\rightarrow n'$ | $(R_{nn'})_{CF}$ ($10^5$ sec$^{-1}$) | $(R_{nn'})_{NG}-(R_{nn'})_{CF}$ ($10^5$ sec$^{-1}$) |
|---|---|---|
| 5→6 | 2.0 | 3.5 |
| 6→7 | 6.0 | 11.1 |
| 6→8 | 1.2 | 4.6 |

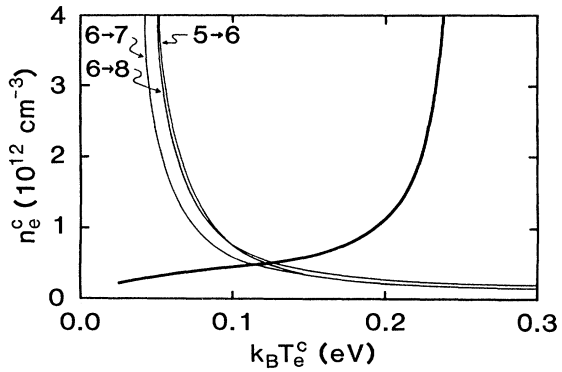


FIG. 3. Electron density vs electron temperature for the low-energy electrons in the negative glow of the 0.846-mA/cm$^2$ discharge at 3.50 Torr. The three light lines arise from the Rydberg-atom diagnostic. The bold line arises from the metastable-atom analysis.

lisional transfers studied.

The metastable-atom diagnostic is carried out under the same discharge conditions as the Rydberg-atom diagnostic. This diagnostic also involves the study of a collision-induced transfer, but in this case the reaction is the exothermic metastable spin conversion reaction of Eq. (1). The transfer rate is determined by mapping the steady-state densities of helium $2\,^1S$ and $2\,^3S$ metastable atoms, and then calculating a fit to the density maps based on an analysis of the metastable transport and kinetics.

The metastable densities are measured by first mapping the relative densities using LIF, and then an absorption measurement is made to put an absolute scale on the maps. The $2\,^1S$ metastable atoms are mapped by driving the $2\,^1S \rightarrow 3\,^1P$ transition at 501.6 nm with the laser and observing $3\,^1D \rightarrow 2\,^1P$ fluorescence at 667.8 nm. The $2\,^3S$ metastable atoms are mapped by driving the $2\,^3S \rightarrow 3\,^3P$ transition at 388.9 nm with the laser and observing $3\,^3S \rightarrow 2\,^3P$ fluorescence at 706.5 nm. Populations of $3p$ and $3d$ levels are coupled by neutral collisions.[16,17] Fluorescence collection and signal processing is the same as for the Rydberg-atom diagnostic except for the substitution of interference filters for the monochromator as a spectral filter.

An absorption measurement is made at the peak of the spatial profile to put an absolute scale on the density maps. The laser is scanned through the same transition used for the LIF while the transmitted laser power is monitored with a photodiode detector. The signal is processed with a boxcar averager and plotted on a stripchart recorder. To simplify the analysis of the absorption line shape the laser power is nonsaturating and the bandwidth is reduced to 500 MHz by the introduction of an extracavity plane parallel étalon. Metastable-atom densities are determined from the integral over frequency of the natural logarithm of the transmittance. Ten absorption measurements are averaged to determine each density. The results of the metastable density measurements are shown as points in Fig. 4.

The net rate for the metastable spin conversion reaction is determined from an analysis of the density maps. The transport and kinetics of $2\,^1S$ and $2\,^3S$ metastable atoms in the discharge are modeled using a pair of balance equations,

$$D_s \frac{\partial^2 M_s}{\partial z^2} - \beta M_s^2 - \beta M_s M_t - \gamma M_s N - \kappa n_e^c M_s + P_s = 0 \ , \quad (7)$$

$$D_t \frac{\partial^2 M_t}{\partial z^2} - \beta M_t^2 - \beta M_s M_t + \kappa n_e^c M_s + P_t = 0 \ , \quad (8)$$

where $M$ is the metastable-atom density, $N$ is the density of the ground-state atoms, $D$ is the diffusion coefficient, $P$ is the production rate per unit volume, $\gamma$ is the rate constant for singlet metastable-atom destruction due to collisions with ground state atoms, $\beta$ is the rate constant for destruction of metastable atoms due to metastable-atom–metastable-atom collisions, $\kappa$ is the rate constant for net destruction of singlet metastable atoms due to low-energy electron collisions, and the $s$ and $t$ subscripts indicate singlet and triplet metastable atoms, respectively. The first three loss terms in each equation are loss terms arising from diffusion and collisions between metastable atoms. There is an additional loss term in the singlet equation arising from collisions with ground-state atoms. The fifth loss term in the singlet equation, and a corresponding gain term in the triplet equation, is due to the spin conversion of metastable atoms. Values of $DN$, $\gamma$, and $\beta$ are taken from Phelps.[18] The temperature dependence of $D$ was taken from Buckingham and Dalgarno[19] and that of $\gamma$ from Allison, Browne, and Dalgar-

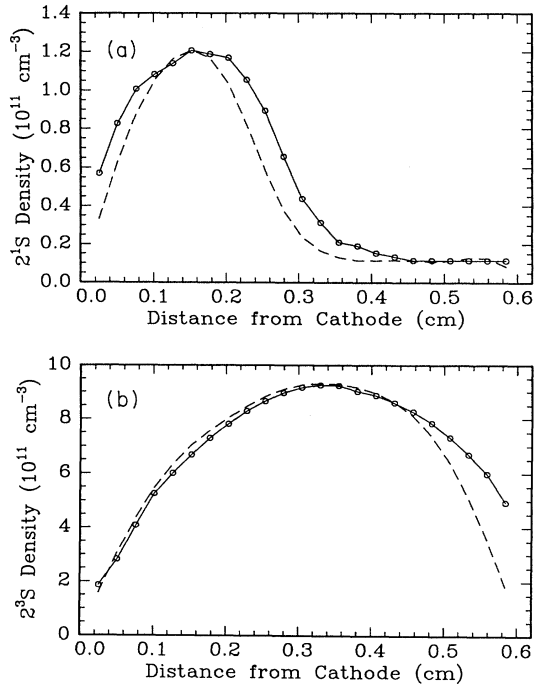


FIG. 4. $2\,^1S$ and $2\,^3S$ metastable-atom densities as a function of distance from the cathode in the 0.846-mA/cm$^2$ discharge. The points are experimental measurements. The dashed curves are calculated densities using the fitting process described in the text.

no.[20] In the original reporting of this diagnostic, there was a small error in the temperature dependence of $D$. The error was $\sim 15\%$ for this discharge, and has been corrected here. The correction did not affect the values of $\kappa n_e^c$ reported in Ref. 7, but did improve agreement between metastable-atom production deduced from the experiment and from Monte Carlo simulations (Fig. 13, Ref. 7).

The coupled equations are solved numerically for $M_s(z)$ and $M_t(z)$ and compared with the experimental results. For the purposes of this model, the spatial dependence of the production terms is assumed to be a fundamental diffusion mode and that of $n_e^c$ a step function: zero in the cathode fall and constant in the negative glow. The assumption about the spatial dependence of the production term is justified by Monte Carlo simulations.[7] Diffusion modes up to tenth order are included in the calculation to describe the spatial asymmetry of the $2\,^1S$ metastable atoms. The values of $P_s$, $P_t$, and $\kappa n_e^c$ are varied until good agreement with the experimental metastable-atom maps is obtained. The experimental maps are more accurate in the center than near the electrodes because of vignetting in the fluorescence collection system and because of fringing of the discharge around the electrode edges. Thus it is most important to reproduce the peak density of the $2\,^1S$ and $2\,^3S$ metastable atoms and the depleted $2\,^1S$ metastable-atom density in the negative glow. The dashed curves in Fig. 4 are the calculated metastable-atom maps. By the method outlined above, $\kappa n_e^c$ is found to be $7\times 10^4$ sec$^{-1}$.

The rate constant for metastable spin conversion $\kappa_m$ was measured by Phelps for room-temperature electrons.[18] The temperature dependence of the rate constant is $(T_e^c)^{-1/2}$ because the cross section scales as the inverse of the electron energy.[21] The value of $\kappa n_e^c$ determined from the metastable analysis must be considered an effective rate for metastable spin conversion since it accounts for both the forward and reverse contributions of reaction (1). Setting $\kappa n_e^c$ equal to the expression for the forward rate minus the reverse rate we obtain

$$\kappa n_e^c = n_e^c \left[ \kappa_m \left[ \frac{0.025\ \text{eV}}{k_B T_e^c} \right]^{1/2} - \left[ \frac{M_t}{3M_s} \right] \kappa_m \left[ \frac{0.025\ \text{eV}}{k_B T_e^c} \right]^{1/2} \times \exp(-0.79\ \text{eV}/k_B T_e^c) \right] . \quad (9)$$

This expression yields a second relation between $n_e^c$ and $T_e^c$ which is plotted as the bold line in Fig. 3. A natural upper bound on $T_e^c$ arises from the above analysis due to the equilibration of reaction (1). The singlets will only be depopulated under the conditions that the forward rate is greater than or nearly equal to the reverse rate.

The two diagnostics discussed above each yield independent relations between $n_e^c$ and $T_e^c$ for the cold electrons in the negative glow. The intersection of these relations, plotted in Fig. 3, yields $n_e^c = 5\times 10^{11}$ cm$^{-3}$ and $k_B T_e^c = 0.12$ eV of the electrons in the negative glow of a 261 V, 0.846 mA/cm$^2$ discharge in 3.50-Torr helium. The uncertainty in the Rydberg-atom diagnostic is primarily due to the uncertainty in the rate coefficient at electron temperatures near the reaction threshold. We estimate this uncertainty to be $-50\%$, $+100\%$. This conservative estimate is based on a comparison by Vriens and Smeets of their rate coefficients with experimental measurements for $n = 13$ to 14 and 15 collision-induced transfer rates for $T_e$ near threshold.[13] The uncertainty in the metastable-atom diagnostic is due mainly to the assumption of a simple two-level system. The collisional and radiative coupling of the $2\,^1S$ with the $2\,^1P$ is not entirely negligible. Particularly the $2\,^1P \rightarrow 2\,^1S$ radiation will be trapped in the cathode fall, but not in the negative glow. The result will be a spatially asymmetric feeding of the $2\,^1S$ population in the negative glow. The effect will be to push the metastable-atom analysis curve to higher $n_e^c$ by as much as a factor of 3.[22] With these uncertainties in mind, the ranges of electron density and temperature consistent with the results of the two diagnostics are $2.5\times 10^{11}$ cm$^{-3} < n_e^c < 8\times 10^{11}$ cm$^{-3}$ and $0.08\ \text{eV} < k_B T_e^c < 0.2$ eV.

Figure 5 shows the empirical values of $n_e^c$ and $k_B T_e^c$ as functions of current density for all discharges studied. Section IV explains why $k_B T_e^c$ depends linearly on current density and why $k_B T_e^c$ is in the 0.1–0.2 eV range.

## III. MONTE CARLO SIMULATIONS

Monte Carlo simulations are used in this work to study the density and energy distribution of hot electrons in the negative glow. This is accomplished by tracking electron

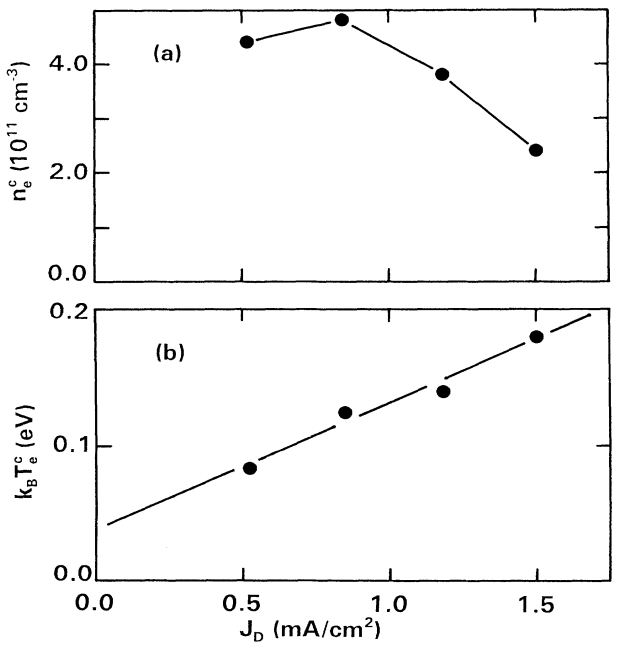


FIG. 5. (a) Density and (b) temperature of the cold negative-glow electrons as functions of discharge current density. The data points are simply connected in (a) and are least-squares fitted to a straight line in (b).

avalanches. Many features of the Monte Carlo simulations are described in Ref. 7, thus only a summary of the method will be presented here, along with additional results used to study the power balance of the negative-glow electrons.

The Monte Carlo simulations are based on empirical gas densities and field distributions measured using opto-galvanic detection of Rydberg atoms.[7] The field at the cathode surface is 1870 V/cm in the 0.846-mA/cm$^2$ discharge. The field decreases linearly with distance from the cathode and extrapolates to zero at a distance of 0.282 cm from the cathode. A uniform (nonreversed) field of 1.0 V/cm is assumed for the negative glow where the actual field is too small to measure. A second simulation is run with a uniform field of 10.0 V/cm in the negative glow to investigate the dependence of the hot-electron density and average energy on the negative-glow field. As expected, the hot electrons are insensitive to the weak negative-glow field. The avalanches start with the emission of an electron from the cathode and end when all of the electrons in the avalanche reach the anode. This approach is not suited for studying the cold trapped electrons in the negative glow because (i) the end of an avalanche could not be defined in terms of all electrons reaching the anode if some electrons became trapped, and (ii) a field reversal or zero is incompatible with the null collision algorithm used in this investigation.[23] (One could conceivably define the end of an avalanche in terms of all hot electrons reaching the anode and all cold trapped electrons fully thermalizing. Such a simulation would be very lengthy.)

The Monte Carlo simulations are three dimensional in the sense that they include angular scattering, but they do not include edge effects due to fringing of the discharge. One-dimensional infinite plane parallel geometry is assumed. Null-collision techniques eliminate most of the time-consuming numerical integration in Monte Carlo simulations. The null-collision technique used in this investigation was developed by Boeuf and Marode for nonuniform fields.[23]

The simulations include anisotropic elastic scattering, excitation to 22 levels, direct ionization, and associative ionization. Total and differential elastic-scattering cross sections are taken from LaBahn and Callaway.[24] Electron-energy loss from elastic recoil is included. The analytic expressions given by Alkhazov for excitation cross sections are used in these simulations.[25] Excitation of singlet and triplet *ns* and *np* levels having *n* from 2 to 5 is included in the simulations. Excitation of singlet and triplet *nd* levels from $n=3$ to 5 is also included. Although some experimental and theoretical information on differential excitation cross sections for electrons on He is available, it is rather limited. Thus we use an isotropic scattering approximation for excitation.

A fraction of the atoms excited to the 3*p* levels and above are associatively ionized. An accurate determination of the fraction requires accurate associative ionization cross sections, cross sections for excitation transfer due to atom and electron collisions, and radiative decay rates. On the basis of what information is available, we estimate that 25% of the atoms excited to the 3*p* levels and above are associatively ionized at 3.5 Torr.[12,16,17] The electrons released in associative ionization contribute to the avalanche; they are assumed to have an initial kinetic energy of 1.0 eV and an isotropic angular distribution. Associative ionization contributes 5–10% of the total ionization. Ionization of metastable atoms due to collisions between pairs of metastable atoms or to electron collisions is not included, but the resulting error is not serious.[7]

The analytic expression given by Alkazov for the total ionization cross section is used in the simulations.[25] His analytic expression for the differential cross section with respect to energy is also used. The angular scattering during ionization is assumed to be such that (i) the incident, scattered, and ejected electrons are coplanar; and (ii) the scattered and ejected-electron velocities are perpendicular with zero net transverse momentum.[23] This approximation for anisotropic scattering in ionizing collisions should be fairly accurate at high energy, and it represents a reasonable attempt to introduce anisotropy in ionizing collisions.

The details of the electron interactions with the cathode and anode must be specified. The kinetic energy of the electrons emitted from the cathode is assumed to be 5.0 eV and they are assumed to have a random angular distribution in the forward direction. The Monte Carlo results are insensitive to the electron distribution at the cathode. It is assumed that all electrons are absorbed immediately on reaching the anode. The neglect of all electron reflection at the anode lowers the hot-electron density in the negative glow near the anode, but the effect on the simulation is visible in the spatial maps and is not too serious.

Some estimate of the accuracy of the simulations is necessary. The empirical map of the cathode fall field is accurate to $\sim 1\%$. Alkhazov's analytic expressions for the electron-He cross sections were based on theoretical and experimental work by many groups.[25] He estimates that the uncertainty is $\pm 25\%$ at low energy and $\pm 5\%$ at high energy where a Born approximation is reliable. We believe his uncertainties are reasonable. Statistical uncertainty is negligible because more than a thousand avalanches are tracked for each complete Monte Carlo simulation. We estimate the total uncertainty of the Monte Carlo results to be $\pm 25\%$.

Figure 6 is the electron density as a function of distance from the cathode as determined from the Monte Carlo simulation. The high density of cold trapped electrons is not included on this plot because the cold trapped electrons are not included in the Monte Carlo simulation. The electrons in the simulation have an average energy substantially greater than 1 eV. Anderson describes such electrons as secondaries and primaries;[2] we identify these electrons as hot electrons. As expected, the density of hot electrons is rather insensitive to the negative-glow field. This field is expected to be in the $\sim 1$-V/cm range or less. An order of magnitude increase in the negative-glow field lowered the negative-glow hot-electron density by $\sim 30\%$. The absolute scale on the density is based on the empirical current balance of 3.13 at the cathode of this 0.846-mA/cm$^2$ discharge.[7] The

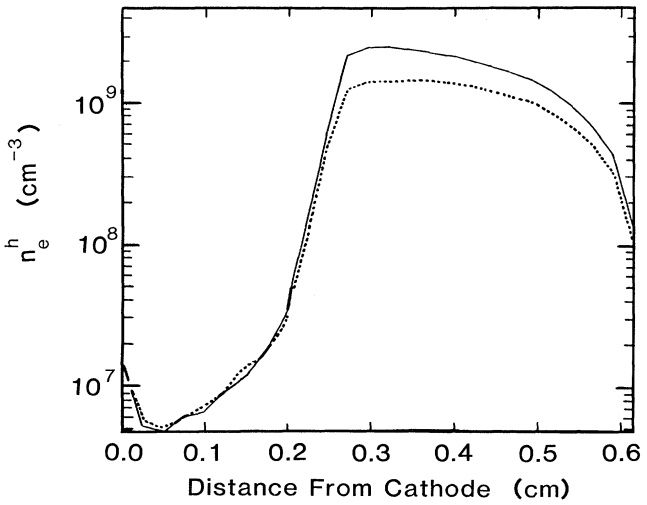


FIG. 6. Density of the hot electrons as a function of distance from the cathode as determined in Monte Carlo simulations. The cold trapped electrons are not included here. The solid curve is from a simulation with a 1.0-V/cm field in the negative glow. The dotted curve is for a 10.0-V/cm field in the negative glow. Both simulations used the same cathode-fall field which is 1870 V/cm at the cathode, decreases linearly with distance from the cathode, and extrapolates to zero at a distance of 0.282 cm from the cathode. This field is measured in the 0.846-mA/cm$^2$ discharge.

current balance, which is the ratio of ion to electron current, has an uncertainty of 20%. The peak hot-electron density in the negative glow of $2.4\times10^9$ cm$^{-3}$ is in rather good agreement with Anderson's probe measurements if one keeps in mind that his discharge conditions are not identical to ours.[2]

Figure 7 is the average kinetic energy $\langle m_e v^2/2\rangle_e$ of the hot electrons as a function of distance from the cathode. These results are independent of the current balance at the cathode, and only weakly dependent on the assumed field in the negative glow. These results are also in rather good agreement with Anderson's probe measurements.[2] The energy-loss rates by hot electrons due to elastic collisions with neutral atoms and due to Coulomb collisions with cold electrons are comparable, but both are unimportant in the power balance of the hot electrons. The average energy of the hot electrons increases only 6% when energy loss due to elastic collisions is removed from the Monte Carlo code. (We show in Sec. IV that energy transfer from the hot electrons to the cold electrons due to Coulomb collisions is important in the power balance of the cold electrons.)

Figure 8 is a histogram in the negative glow (0.418 cm

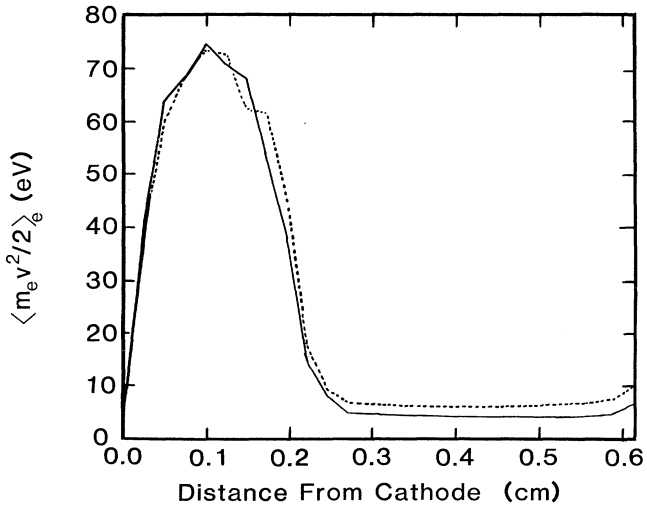


FIG. 7. Average kinetic energy of the hot electrons as a function of distance from the cathode determined in Monte Carlo simulations for the 0.846-mA/cm$^2$ discharge. Note that an order of magnitude increase in the negative glow field from 1.0 V/cm (solid curve) to 10.0 V/cm (dotted curve) only increased the average energy in the negative glow by ~33%.

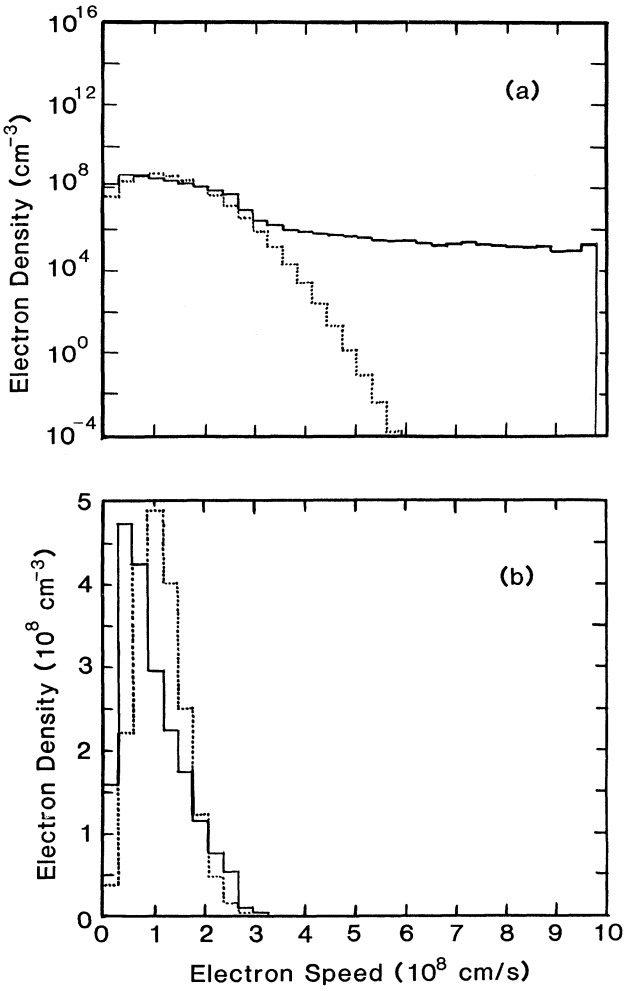


FIG. 8. Histogram of the speed distribution of the hot electrons in the negative glow of the 0.846-mA/cm$^2$ discharge. The solid line is from the Monte Carlo simulation with a 1.0-V/cm field in the negative glow. The dotted line is a Maxwellian speed distribution for the same density and average energy. The cutoff of the Monte Carlo histogram corresponds to the maximum electron energy, which is determined by the discharge voltage. (a) Semilogarithmic plot. (b) Linear plot.

from the cathode) of the speed distribution $\int f_e 2\pi v^2 d\mu$, where $f_e$ is the full phase-space electron distribution, $v$ is the speed, and $\mu$ is the cosine of the angle between the electron velocity and discharge axis. This histogram is from a simulation with a 1.0-V/cm field in the negative glow. A Maxwellian speed distribution normalized to the same density and for a corresponding electron temperature ($k_B T_e^h = \frac{2}{3}\langle m_e v^2/2\rangle_e = 3.05$ eV) is included on the plot. The Monte Carlo distribution peaks at lower speed and has an excess of high-speed electrons in comparison to the Maxwellian. The energy transfer rate due to Coulomb collisions has a rather weak energy dependence, which justifies an approximation in Sec. IV. These hot electrons are approximated as Maxwellian in a calculation of energy transfer to the cold electrons during Coulomb collisions.

## IV. POWER BALANCE

In this section different terms in the power balance of the cold negative-glow electrons are explored. Power loss or the cooling rate is calculated for two processes: elastic collisions with neutral atoms and Coulomb collisions with ions. Power gain or the heating rate is also calculated for two processes: Coulomb collisions with hot electrons and superelastic collisions with metastable atoms. All cooling and heating rates will be calculated per cold electron and expressed in units of eV/sec. Where necessary experimental results such as the density ($n_e^c = 5\times10^{11}$ cm$^{-3}$) and the temperature ($k_B T_e^c = 0.12$ eV) of the cold negative-glow electrons in the 0.846-mA/cm$^2$ discharge are used. Monte Carlo simulations are used to determine the density and average energy of the hot negative-glow electrons.

The fraction of the electron kinetic energy transferred due to recoil in an elastic collision with a neutral atom at rest is $2(1-\cos\theta)m_e/m_0$, where $m_e$ is the electron mass, $m_0$ is the atom mass, and $\theta$ is the scattering angle. Thus the elastic-energy-transfer cross section is proportional to the momentum-transfer cross section $\sigma_{\rm MT}$, which is almost independent of energy for low-energy electrons on He atoms. The momentum-transfer cross section is $6.6\times10^{-16}$ cm$^2$ for 1-eV and $6.5\times10^{-16}$ cm$^2$ for 4-eV electrons on He.[24] Precision swarm experiments by Crompton, Elford, and Robertson indicate that $\sigma_{\rm MT}$ decreases slightly for electron energies below 1 eV; a value of $6\times10^{-16}$ cm$^2$ is used.[26] Assuming a Maxwellian electron-energy distribution and neglecting the thermal motion of the atoms, the cooling rate per electron is

$$8\sigma_{\rm MT} N (k_B T_e^c)^{3/2}\sqrt{2m_e}/(m_0\sqrt{\pi}) ,$$

where $N$ is the neutral-atom density of $1.03\times10^{17}$ cm$^{-3}$. This expression yields a cooling rate of $9.4\times10^4$ eV/sec.

If the effect of a nonzero gas temperature ($k_B T = 0.028$ eV) is included, then the cooling rate is

$$8\sigma_{\rm MT} N (k_B T_e^c - k_B T)(2k_B T_e^c/m_e + 2k_B T/m_0)^{1/2} \times m_e m_0/[(m_e+m_0)^2\sqrt{\pi}] .$$

The derivation of this formula is straightforward but somewhat tedious. It yields a cooling rate per electron of $7.2\times10^4$ eV/sec.

The cooling rate for Coulomb collisions of electrons with ions

$$4\sqrt{2\pi} n_e^c e^4 (k_B T_e^c - k_B T_i)(m_0 k_B T_e^c + m_e k_B T_i)^{-3/2} \times \sqrt{m_e m_0}\ln(2/\theta_m)$$

is derived by Longmire.[27] Here $\ln(2/\theta_m)$ is taken to be 10, the ion temperature $T_i$ is the same as the gas temperature, and $e$ is the unit charge. A cold electron in the negative glow loses $1.3\times10^4$ eV/sec in Coulomb collisions with ions.

The heating rate due to Coulomb collisions between hot electrons and cold electrons is

$$4\sqrt{2\pi} n_e^h e^4 (k_B T_e^h - k_B T_e^c)(k_B T_e^h + k_B T_e^c)^{-3/2} \times \ln(2/\theta_m)/\sqrt{m_e}$$

as derived by Longmire.[27] The hot-electron density ($n_e^h = 1.56\times10^9$ cm$^{-3}$) and temperature ($k_B T_e^h = 3.05$ eV) are spatial averages over the negative glow of the Monte Carlo results from Sec. III. The hot electrons, which are somewhat non-Maxwellian, are here approximated as Maxwellian with $k_B T_e^h$ equal to $\frac{2}{3}$ of their average kinetic energy. The heating rate per cold electron is $7.1\times10^4$ eV/sec.

Superelastic collisions of cold electrons with metastable atoms provide some heating of the cold electrons. Collisions in which metastable atoms are de-excited to the ground state are not important. The rate constants of a few $10^{-9}$ cm$^3$/sec to $10^{-8}$ cm$^3$/sec are small in comparison with other rate constants; furthermore, the outgoing electron has $\sim$20 eV of kinetic energy.[28] This energetic electron will escape from the negative glow before it shares a significant fraction of its kinetic energy with the cold electrons through Coulomb collisions. The metastable-atom spin conversion reaction of Eq. (1) is a more effective, but not dominant, heating mechanism for the cold electrons. For electrons at ambient temperature ($k_B T_e = 0.026$ eV), the rate constant of this reaction is $3.2\times10^{-7}$ cm$^3$/sec.[18] This reaction does severely suppress the singlet metastable-atom density in the negative glow. The empirical singlet metastable-atom density $M_s$ and effective reaction rate $\kappa n_e^c$, which includes the reverse reaction, are used to estimate the heating rate per cold electron 0.79 eV $M_s \kappa n_e^c / n_e^c$. This expression yields $0.13\times10^4$ eV/sec.

The power balance of the cold negative-glow electrons is dominated by cooling due to energy loss in elastic collisions with neutral atoms and by heating due to energy gain in Coulomb collisions with hot electrons in the negative glow. Monte Carlo simulations for other current densities indicate that the hot-electron density increases linearly with discharge current density. This explains why $k_B T_e^c$ increases linearly with current density and extrapolates to $k_B T$ (gas temperature) at low current densities as shown in Fig. 5.

## V. LIGHT FROM THE NEGATIVE GLOW

The negative-glow region is typically an order of magnitude or more brighter than the cathode-fall region (Crookes dark space) in a cold cathode glow discharge. The combination of (i) a detailed distribution function for hot negative-glow electrons, (ii) the spatial maps of the absolute metastable-atom densities from the experiment,[7] and (iii) recently measured electron-impact cross sections for excitation from the $2\,^3S$ metastable level to higher levels,[29] is used in this section to assess the role of multistep excitation in producing light from the negative glow. Multistep excitation is important in the negative glow. Electron-ion recombination is not required to explain the brightness of the negative glow.

One of the strongest visible lines in the He *I* spectrum is the line at 587.6 nm from the $3\,^3D$ level. This level decays only by the 587.6-nm transition to the $2\,^3P$ level. In this discussion excitation transfer to and from the $3\,^3D$ level from and to other nearby levels will be neglected. The calculated single-step and single-step plus two-step excitation rates per unit volume are shown in Fig. 9. The only important two-step excitation process is from the $2\,^3S$ metastable level, because the density of $2\,^1S$ metastable atoms in the negative glow is far lower.

The single-step excitation rate per unit volume is only slightly asymmetric about the cathode-fall–negative-glow boundary. This slight asymmetry is due to the sharp peak in the energy dependence of the cross section just above threshold. The energy dependence is typical of cross sections for spin changing collisions, such as this $3\,^3D$ excitation from the $1\,^1S$ level. The single-step excitation rates per unit volume of the singlet He levels and the ionization rate per unit volume are even more symmetric about the cathode-fall–negative-glow boundary. Thus single-step excitation cannot explain the fact that the negative-glow region is much brighter than the cathode-fall region.

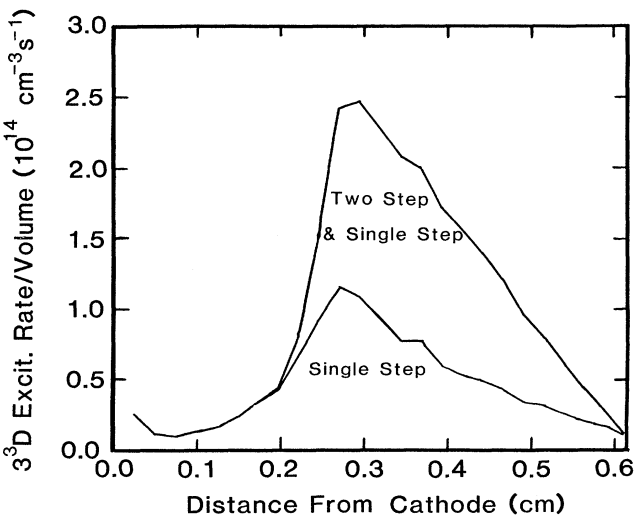


FIG. 9. Excitation rate per unit volume of He atoms to the $3\,^3D$ level as a function of distance from the cathode in the 0.846-mA/cm$^2$ discharge. The lower curve includes only (single-step) excitation from the ground-state level. The upper curve includes excitation from the ground-state level and (two-step) excitation from the $2\,^3S$ metastable level.

The inclusion of two-step excitation from the $2\,^3S$ metastable level produces an excitation rate per unit volume that is very asymmetric about the cathode-fall–negative-glow boundary. The calculated excitation rate per unit volume in the negative glow peaks at a value 20 times greater than the minimum in the cathode-fall region.

These results indicate that electron-ion recombination in the negative glow is not required to explain the greater brightness of the negative glow in comparison with the cathode-fall region. We have argued in the past that if the electron temperature is significantly above gas temperature, then recombination is not an important term in the ionization (particle) balance of the negative glow.[7] The rate per unit volume of electron collisionally stabilized electron-ion recombination scales as $(n_e^c)^3(T_e^c)^{-4.5}$.[30] The strong temperature dependence reduces the importance of electron-stabilized recombination. Nevertheless, at least some electron-ion recombination does occur in the negative glow. The observation of $He_2$ emission bands is convincing evidence for electron-ion recombinations.[7] Electron-ion recombination in He, especially dissociative recombination of $He_3^+$ and $He_4^+$, has been the subject of controversy in the past; some lingering concern remains that mechanisms may not be completely understood.[31] Our experiments and simulations indicate that electron-ion recombination is not important in the ionization balance of the negative glow and is not needed to explain the greater brightness of the negative glow in comparison with the cathode-fall region.

## VI. SUMMARY, CONCLUSION, AND FUTURE WORK

The density ($n_e^c \cong 5\times10^{11}$ cm$^{-3}$) and temperature (0.1 eV $\leq k_B T_e^c \leq$ 0.2 eV) of the cold electrons in the negative glow of a clean He glow discharge are determined using laser spectroscopy. Rates for both inelastic and superelastic collision of cold electrons with excited atoms are measured using laser-induced fluorescence and absorption spectroscopy. The density and temperature of the cold electrons are determined from these rates. These cold electrons are trapped in a potential-energy well in the negative glow.

In a complementary investigation, the hot-electron density ($n_e^h \cong 10^9$ cm$^{-3}$) and temperature ($k_B T_e^h \simeq 3$ eV) are determined from Monte Carlo simulations and the measured cathode-fall electric field. The hot electron density, the hot-electron temperature, and the cold-electron density are essentially in agreement with probe and microwave measurements by Anderson.

The power balance of the cold electrons is analyzed by combining results from the experiments and Monte Carlo simulations. The power balance of the cold electrons is dominated by cooling due to recoil during elastic collisions with neutral atoms and by heating due to Coulomb collisions with hot electrons injected into the negative glow from the cathode-fall region. The cold-electron temperature is found to be in the 0.1- to 0.2-eV

range and to vary linearly with discharge current density because of a linear variation of hot-electron density with discharge current density. Although the extremely good agreement between heating and cooling found in our analysis of the power balance of the cold electrons may be somewhat fortuitous, there is no doubt that Coulomb scattering will maintain the cold-electron temperature well above gas temperature in the discharge studied here.

Two-step excitation of radiating levels (via the $2\,^3S$ metastable level) causes the greater brightness of the negative glow in comparison with the cathode-fall region. Electron-ion recombination is not needed to explain the enhanced atomic He emission from the negative glow, but is needed to explain the molecular $He_2$ emission from the negative glow. Published electron-ion recombination rate constants, when combined with the measured cold-electron densities and temperatures, indicate that electron-ion recombination is not an important term in the ionization balance of the negative glow.

The goal of this investigation is to identify the most important physical processes in a typical negative glow. These processes must be included in plasma simulations such as those based on the convective scheme. A fully self-consistent kinetic model of the cathode-fall region based on the convective scheme has been reported.[9] This cathode-fall model is based on the assumption of negligible ion current at the cathode-fall–negative-glow boundary. It is very desirable to relax this assumption and to use the convective scheme through the negative glow to the anode surface. Such calculations are already showing the expected field reversal. Electrode-to-electrode models of discharge plasmas which are fully self-consistent and kinetic will provide genuine predictive capability.

## ACKNOWLEDGMENTS

We are grateful to Dr. T. J. Sommerer for his work on convective scheme simulations of these plasmas.

[1]E. A. Den Hartog, T. R. O'Brian, and J. E. Lawler, Phys. Rev. Lett. **62**, 1500 (1989).
[2]J. M. Anderson, J. Appl. Phys. **31**, 511 (1960).
[3]G. Francis, in *Gas Discharges II,* Vol. 22 of *Handbuch der Physik,* edited by S. Flügge (Springer-Verlag, Berlin, 1956), p. 53.
[4]K. G. Emeleus, J. Phys. D **14**, 2179 (1981).
[5]W. H. Long, Northrup Research and Technology Center, Technical Report No. AFAPL-TR-79-2038, 1978. (Available as Doc. No. ADA 070 819 from the National Technical Information Service, Springfield, VA 22161.)
[6]M. J. Druyvesteyn, Physica **4**, 669 (1937).
[7]E. A. Den Hartog, D. A. Doughty, and J. E. Lawler, Phys. Rev. A **38**, 2471 (1988).
[8]R. A. Gottscho, A. Mitchell, G. R. Scheller, Y.-Y. Chan, and D. B. Graves, Phys. Rev. A **40**, 6407 (1989).
[9]T. J. Sommerer, W. N. G. Hitchon, and J. E. Lawler, Phys. Rev. A **39**, 6356 (1989).
[10]T. J. Sommerer, W. N. G. Hitchon, and J. E. Lawler, Phys. Rev. Lett. **63**, 2361 (1989).
[11]T. F. Gallagher, S. A. Edelstein, and R. M. Hill, Phys. Rev. A **15**, 1945 (1977).
[12]W. L. Wiese, M. W. Smith, and B. M. Glennon, *Atomic Transition Probabilities,* Natl. Bur. Stand. Ref. Data Ser., Natl. Bur. Stand. (U.S.) Circ. No. 4 (U.S. GPO, Washington, DC, 1966), Vol. I.
[13]L. Vriens and A. H. M. Smeets, Phys. Rev. A **22**, 940 (1980).
[14]W. C. Martin, Phys. Rev. A **36**, 3575 (1987).
[15]A. Kono and S. Hattori, Phys. Rev. A **29**, 2981 (1984).
[16]H. F. Wellenstein and W. W. Robertson, J. Chem. Phys. **56**, 1072 (1972); **56**, 1077 (1972).
[17]B. Dubreuil and A. Catherinot, Phys. Rev. A **21**, 188 (1980).
[18]A. V. Phelps, Phys. Rev. **99**, 1307 (1955).
[19]R. A. Buckingham and A. Dalgarno, Proc. R. Soc. London Ser. A **213**, 506 (1952).
[20]D. C. Allison, J. C. Browne, and A. Dalgarno, Proc. Phys. Soc. London **89**, 41 (1966).
[21]W. C. Fon, K. A. Berrington, P. G. Burke, and A. E. Kingston, J. Phys. B **14**, 2921 (1981).
[22]E. A. Den Hartog, Ph.D. thesis, University of Wisconsin, Madison, 1989 (unpublished).
[23]J. P. Boeuf and E. Marode, J. Phys. D **15**, 2169 (1982).
[24]R. W. LaBahn and J. Callaway, Phys. Rev. A **2**, 366 (1970); Phys. Rev. **180**, 91 (1969); **188**, 520 (1969).
[25]G. D. Alkhazov, Zh. Tekh. Fiz. **40**, 97 (1970) [Sov. Phys.—Tech. Phys. **15**, 66 (1970)].
[26]R. W. Crompton, M. T. Elford, and A. G. Robertson, Aust. J. Phys. **23**, 667 (1970).
[27]C. L. Longmire, *Elementary Plasma Physics* (Wiley, New York, 1963), p. 204.
[28]R. K. Nesbet, *Variational Methods in Electron-Atom Scattering Theory* (Plenum, New York, 1980), p. 188.
[29]D. L. A. Rall, F. A. Sharpton, M. B. Schulman, L. W. Anderson, J. E. Lawler, and C. C. Lin, Phys. Rev. Lett. **62**, 2253 (1989).
[30]R. Deloche, P. Monchicourt, M. Cheret, and F. Lambert, Phys. Rev. A **13**, 1140 (1976).
[31]J. F. Delpech, J. Boulmer, and J. Stevefelt, in *Advances in Electronics and Electron Physics,* edited by L. Marton (Academic, New York, 1975), Vol. 39, p. 121.